ACS central science

Research Article

Cite This: ACS Cent. Sci. 2018, 4, 929−937

In Situ Coupling of Multidimensional MOFs for Heterogeneous Metal-Oxide Architectures: Toward Sensitive Chemiresistors

Ji-Soo Jang, Won-Tae Koo, Dong-Ha Kim, and Il-Doo Kim*

Department of Materials Science and Engineering, Korea Advanced Institute of Science and Technology, 291 Daehak-ro, Yuseong-gu, Daejeon 305-701, Republic of Korea

Advanced Nanosensor Research Center, KI Nanocentury, Korea Advanced Institute of Science and Technology, 291 Daehak-ro, Yuseong-gu, Daejeon 34141, Republic of Korea

Supporting Information

ABSTRACT: Metal−organic frameworks (MOFs) are used as a new intriguing class of templates, which enable the creation of porous inorganic nanostructures via calcination. In this work, we first introduce in situ coupling of multidimensional MOFs for producing heterogeneous metal-oxide composite with multiple p−n junctions. Controlling relative ratios of two mixed solvents (water and ethanol), in zeolitic imidazolate framework (ZIF) growth, leads to the distinctive morphological evolution such as rod, sheet, and polyhedron particles. One-pot hybridization of ZIF-8 (sheet) with ZIF-67 (rods) results in the generation of hierarchically assembled 1D ZIF-67 rods anchored on a 2D ZIF-8 sheet. Through the calcination of such hybridized ZIFs, we successfully prepared hierarchically assembled 1D Co_3O_4 rods immobilized in a 2D ZnO sheet, possessing numerous n-type ZnO/p-type Co_3O_4 heterogeneous interfaces. This unique structure offers a remarkably enhanced chemiresistive sensing performance (R_a/R_g = 29 at 5 ppm acetone).

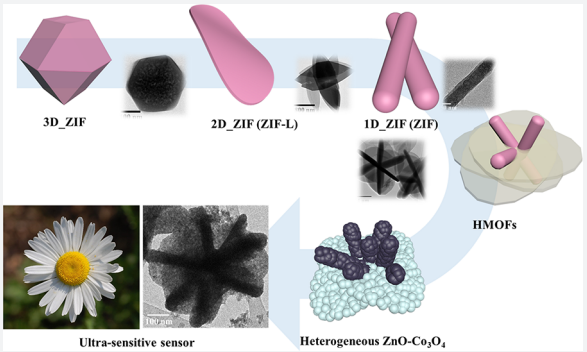

Metal−organic frameworks (MOFs), which are built under the coordination of metal nodes and organic linkers, have been intensively explored as promising precursor materials.[1] For example, various functional materials, ranging from organic to inorganic materials (metal oxides, metal nitride, metal sulfide, and metal phosphide), have been synthesized by using various MOF precursors, which enable a wide range of applications including catalysis,[2−5] capture of gases,[6] energy storage,[7,8] drug delivery,[9] and chemical sensors.[10] In particular, microstructures, porosity, and morphologies of MOFs can be easily tailored for desired applications by assembling various types of metal nodes and organic linkers. For instance, Guo et al. developed various morphologies of MIL-53 (Fe-based MOFs) from yolk−shell octahedron to nanorod, by controlling the coordination of Fe ions and H_2BDC linkers via microwave-assisted synthesis. Various morphologies of the MIL-53 lead to the formation of high-surface-area Fe_2O_3 architectures after calcination, particularly optimized as high-performance anode materials for lithium ion batteries.[11] Tang et al. developed the ultrathin NiCo bimetallic MOFs nanosheets, which exhibited great electrocatalytic activity.[12]

More recently, for further improvement in the functionalities of MOF-derived materials, the hierarchical MOF architectures have been exploited. Representatively, Guan et al. developed hierarchical Fe−carbon composite materials by templating hybridized dual-MOFs (MIL-88B and ZIF-8; ZIF, zeolitic imidazolate framework),[13] exhibiting superior catalytic performance. However, the synthesis of multidimensional hybrid MOFs by a simple one-pot process and their sacrificial templating route for creation of heterogeneous hybrid oxide architectures have rarely been investigated.

Chemiresistive gas sensors have recently attracted much attention due to increasing demands for monitoring hazardous gases including acetone, hydrogen sulfide, toluene, and nitrogen dioxide.[14,15] Among the various sensitive sensing materials, noble-metal-catalyst-decorated semiconducting metal oxides (SMOs) have been regarded as the best sensing layers, showing superior sensing performances.[16,17] However, in the case of high-temperature-operating SMO gas sensors, metal catalysts are often degraded after long cycled operation, which is detrimental to long-term device stability. As a cost-effective and more reliable approach, the heterogeneous hierarchical metal-oxide nanomaterials, which possess high surface area, high porosity, and electronically sensitized multiheterojunction structures, have been intensively exploited as promising sensing layers. However, the simple and mass-productive fabrication of such materials is still challenging; thus, a new synthetic approach for the rational designing of multiheterojunction structures with high surface area and open porosity is required.

Received: June 6, 2018
Published: June 29, 2018

DOI: 10.1021/acscentsci.8b00359
ACS Cent. Sci. 2018, 4, 929−937

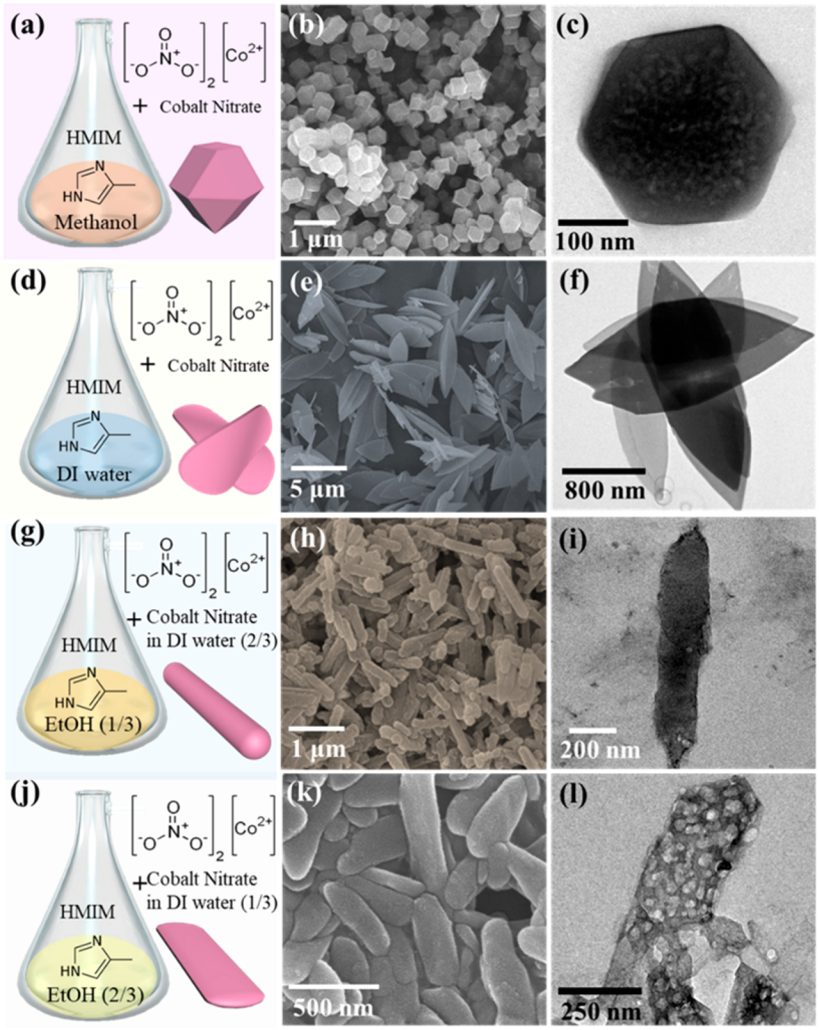

Figure 1. Schematic illustration of synthetic strategy of (a) ZIF-67, (d) Co-based ZIF-L, (g) ZIF-67 rods, and (j) ZIF-67 belts. Corresponding SEM images of (b) ZIF-67, (e) Co-based ZIF-L, (h) ZIF-67 rods, and (k) ZIF-67 belts. TEM images of (c) ZIF-67, (f) Co-based ZIF-L, (i) ZIF-67 rods, and (l) ZIF-67 belts.

In this work, we designed hybrid MOFs (HMOFs), i.e., one-dimensional (1D) rod-shaped MOFs anchored to two-dimensional (2D) sheet-shaped MOFs, as a new sacrificial template for direct synthesis of a hierarchical metal-oxide composite with abundant p−n heterojunctions, which are suitable for highly sensitive chemiresistors. Upon the simple control of the relative ratio of two mixed solvents, the ZIF-67 (Co-ion-based MOF) with various morphologies, including polyhedron, sheet, rod, and belt, was successfully synthesized. Furthermore, the in situ coupling of 1D rodlike ZIF-67 and 2D sheetlike ZIF-8 resulted in the creation of daisy-flower-like composite MOF structures. Through simple calcination of the HMOFs, hierarchically assembled 1D Co_3O_4 rods functionalized on 2D ZnO sheets were formed and used as superior acetone-sensing layers.

RESULTS AND DISCUSSION

Various morphologies of ZIF-67, i.e., polyhedron (ZIF-67), sheets (ZIF-L), rods (ZIF-67 rods), and belts (ZIF-67 belts), are tailored by controlled manipulation of a single solvent and/or cosolvents used for MOF growth (Figure 1). When the weight ratio of HMIM/Co precursors dispersed in methanol is 2.16, the polyhedral ZIF-67 structure with uniform size distribution of 300−400 nm is generally formed by the assembly of Co ions and 2-methylimidazole (HMIM) organic linkers (Figure 1a−c), which has been introduced in the previous literature.[10] On the other hand, the ZIF-67 assembled in deionized (DI) water exhibits flat leaf-shaped Co-based ZIF-L structures (Figure 1d). As shown in the SEM image of Figure 1e and TEM image of Figure 1f, Co-based ZIF-L structures with leaf shapes are well-formed by 2D networking between Co ions and HMIM linkers.[18] To further engineer the microstructure and morphology of ZIF-67, we employed the cosolvent system of DI water and ethanol (EtOH) with two different volume ratios (v/v), i.e., DI water/EtOH = 13:27 (≈1:2) and 27:13 (≈2:1). Interestingly, when the HMIM organic linkers dissolved in EtOH (27 mL) are mixed with Co ions dissolved in DI water (13 mL), the rod-shaped ZIF-67 (ZIF-67 rods) was created (Figure 1g). As shown in Figure 1h, the elongated ZIF-67 rods had micron-sized length (∼5 μm) and mean width of 255.83 nm. The TEM image of ZIF-67 rods (Figure 1i) exhibits dense rod structures without any macrosized (>50 nm) pores. On the other hand, in the case of using a mixed solvent with volume ratio of DI water (2)/EtOH (1), the belt-shaped ZIF-67 (ZIF-67 belts) structures were formed (Figure 1j,k). Moreover, numerous macrosized

DOI: 10.1021/acscentsci.8b00359
ACS Cent. Sci. 2018, 4, 929−937

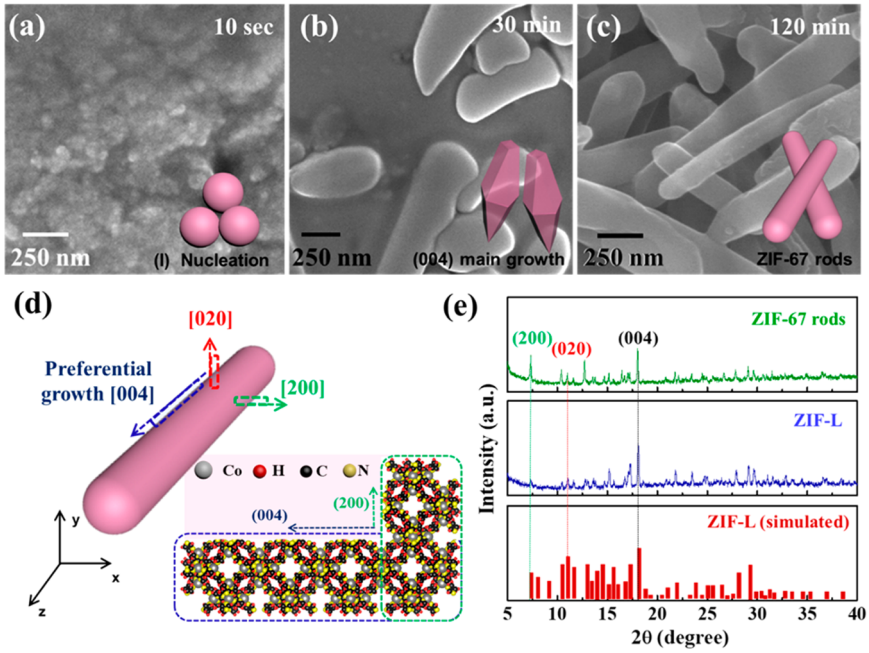

Figure 2. Ex situ SEM analysis of ZIF-67 rods grown for (a) 10 s, (b) 30 min, and (c) 120 min. (d) Schematic illustration of the growth process for ZIF-67 rods with growth mechanism. (e) XRD patterns of ZIF-67 rods and Co-based ZIF-L.

pores were created in the inner side of ZIF-67 belts (TEM image of Figure 1l). Our observation revealed that the dimension and shape of ZIF-67 can be tailored by varying the ratio of two mixed solvents even in constant weight ratio of HMIM/Co precursors.

The EDS mapping analysis of ZIF-67 rods and ZIF-67 belts indicated that Co, C, N, and O components were uniformly distributed in both ZIF-67 rods and ZIF-67 belt structures (Figure S1b,d of the Supporting Information). The STEM image clearly revealed the existence of high-density macropores within belt-shaped ZIF-67 (Figure S1c of the Supporting Information). To investigate the formation process of ZIF-67 rods, we carried out the ex situ SEM analysis for each specimen obtained under different growth times, i.e., 10 s, 30 min, and 120 min. As shown in Figure 2a, the nanoscale particles with mean size of 46.21 nm were first formed after mixing of HMIM-dissolved EtOH (1/3 vol %) with cobalt-nitrate-dissolved DI water (2/3 vol %) for 10 s. After continued stirring for 30 min, the elongated ZIF-67 with flat shape was achieved (Figure 2b). Finally, ZIF-67 rods were formed after 120 min (Figure 2c). The creation of ZIF-67 rods might be attributed to the preferred growth of nucleated ZIF-67 particles along the [004] direction while the growth along the [020] and [200] direction was relatively suppressed (Figure 2d). To investigate the preferential growth direction of ZIF-67 rods, we carried out powder X-ray diffraction (PXRD) analysis (Figure 2e). Similar to Co-based ZIF-L, the relatively strong (004) peak intensity was observed along with weak (020) and (200) peaks. Thus, ZIF-67 rods preferentially grew along the [004] direction (blue dotted boxes in Figure 2d). To verify the degree of ZIF-67 rod orientation, we calculated the crystallographic preferred orientation (CPO) by evaluating the relative peak intensity of (004), (020), and (200). As a result, the $CPO_{(020)/(004)}$ value for ZIF-67 rods was 0.771, which was much higher compared with that (0.41) for Co-based ZIF-L. In addition, the $CPO_{(200)/(004)}$ for ZIF-67 rods (0.867) was also higher than that of Co-based ZIF-L (0.362). The increased $CPO_{(020)/(004)}$ and $CPO_{(200)/(004)}$ for ZIF-67 rods indicates that the growth along the [020] and [200] direction occurs more dominantly compared with Co-based ZIF-L, resulting in the formation of a rodlike morphology. Furthermore, regardless of type of ions involved (Zn or Co ions), ZIF-L showed the same crystalline behavior because they have the same XRD peak properties (Figure S2 of the Supporting Information).

The growth mechanism of ZIF-67 rods can be explained on the basis of (i) different degrees of HMIM deprotonation and (ii) the Marangoni flow effect. First, in the viewpoint of deprotonation of HMIM, when Co ions react with HMIM linkers dispersed in DI water, the outer side of tetragonal $[CoN_4]$ in Co-based ZIF-L consists of one free MIM and three Co−MIM bonds, showing elongated Co-based ZIF-L structures. Thus, DI water tends to restrain the [200] and [020] growth of ZIF-67.[18,19] On the other hand, methanol induces the binding of four organic linkers with Co, showing polyhedron structures.[18] That is, the different degree of HMIM deprotonation is a critical factor for the binding state of Co−MIM bonds. As shown in Table S1 of the Supporting Information, the pH values of solutions used for the growth of ZIF-67 rods (pH = 8.05) and ZIF-67 belts (pH = 8.22) were slightly lower than that of DI water (pH = 8.47). Considering that DI water with a high pH value leads to suppressed [200] and [020] growth of ZIF-67, the reduction of pH level in mixed solution, i.e., DI water/EtOH = 1:2 and 2:1, induces relatively weaker suppression in [020] and [200] growth; this is well-matched with the XRD results of ZIF-67 rods.

Regarding the Marangoni flow effect, when EtOH solution is mixed with DI water (Figure S3 of the Supporting Information), the Marangoni flow can be formed at the interface between DI water and EtOH because of the difference in surface energy (γ_{water}, 77 mN/m; and γ_{EtOH}, 22 mN/m).[20] Because of the creation of a surface tension gradient between DI water and EtOH, the fluidic flow from EtOH to DI water spontaneously occurs, enabling the one-dimensional (1D) alignment of HMIM into the Co-ion-dissolved DI water.

DOI: 10.1021/acscentsci.8b00359
ACS Cent. Sci. 2018, 4, 929−937

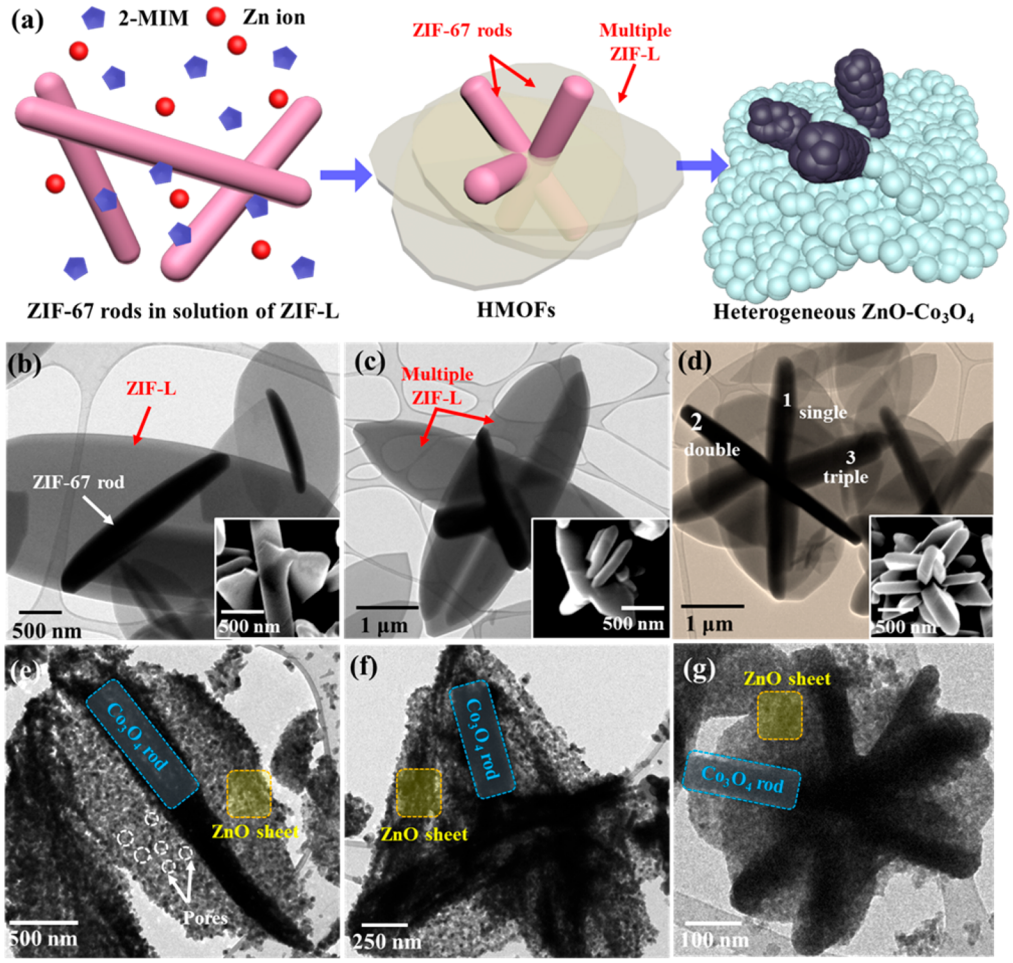

Figure 3. (a) Schematic illustration of the synthetic process for heterogeneous HMOF and HMOF-templated heterogeneous ZnO−Co_3O_4 hierarchical composite structures. TEM images with inset of corresponding SEM image: (b) single-ZIF-L@ ZIF-67 rods, (c) double-ZIF-L@ZIF-67 rods, and (d) triple-ZIF-L@ZIF-67 rods. TEM images of (e) single-Co_3O_4 rods@ZnO sheet, (f) double-Co_3O_4 rods@ZnO sheet, and (g) triple-Co_3O_4 rods@ZnO sheet.

Similarly, Cai et al. reported that the polystyrene nanoparticles can be aligned by the Marangoni flow in the EtOH/water cosolvent system.[20] As a control experiment, when both Co nitrate and HMIM powders were simultaneously dissolved in the cosolvents (EtOH and DI water), the conventional polyhedral ZIF-67 structures were formed (Figure S6 of the Supporting Information). These results further support that the formation of ZIF-67 rods and ZIF-67 belt structures is greatly affected by the Marangoni flow effect.

To prepare hierarchically assembled metal-oxide structures with numerous p−n heterojunctions, we calcined sequentially grown hybrid MOF templates (HMOFs) at 450 °C (Figure 3a).[21,22] Considering the grain sizes and hierarchical structures, we selected 450 °C as the optimized calcination temperature. It is noted that the lower temperature (350 °C) as compared to 450 °C cannot induce crystallinity in ZnO−Co_3O_4 structures (Figure S4 of the Supporting Information). On the other hand, using the Scherrer equation, it was observed that higher calcination temperatures, i.e., 550, 650, and 750 °C, resulted in larger grain sizes (53.6, 69.5, and 92.7 nm, respectively), compared with that (31.7 nm) of the 450 °C calcined double-Co_3O_4 rods@ZnO sheet (Table S2 of the Supporting Information), thereby leading to degraded sensitivity to target gas molecules, in accordance with previous studies.[23,24] More importantly, a higher calcination temperature resulted in the agglomeration of nanostructures and collapsed hierarchical structures of the double-Co_3O_4 rods@ZnO sheet (Figure S5 of the Supporting Information). Therefore, we chose 450 °C as the optimized calcination temperature for HMOFs to achieve well-developed nanostructures with small grain size. The Co-based ZIF-67 rods were grown as the first seed layer, and Zn-based ZIF-L was subsequently formed as the second layer on the ZIF-67 rods. It is noted that the Zn-based ZIF-L can also be formed by following the synthetic process used for growth of Co-based ZIF-L (Figure S7 of the Supporting Information). Since Zn-based ZIF-L-derived thin-layered metal-oxide structures induce the effective modulation of the electron depletion region, they are highly suitable as the chemiresistive-type gas sensing layer.[25,26] In the case of using macroporous ZIF-67 belts as the first seed layer, calcined structures collapsed because of weak morphological stability caused by numerous pores (Figure S8 of the Supporting Information) that existed within ZIF-67 belts (Figure S1c of the Supporting Information). Thus, we used ZIF-67 rods with high structural stability as a seed layer for subsequent growth of Zn-based ZIF-L, enabling multi-dimensionally assembled 1D−2D structures. During the HMOF formation process, the 2D Zn-based ZIF-L was grown on the facet of the 1D ZIF-67 rods, forming 1D ZIF-67-rod-embedded Zn-based ZIF-L (hereafter, ZIF-L@ZIF-67

DOI: 10.1021/acscentsci.8b00359
ACS Cent. Sci. 2018, 4, 929−937

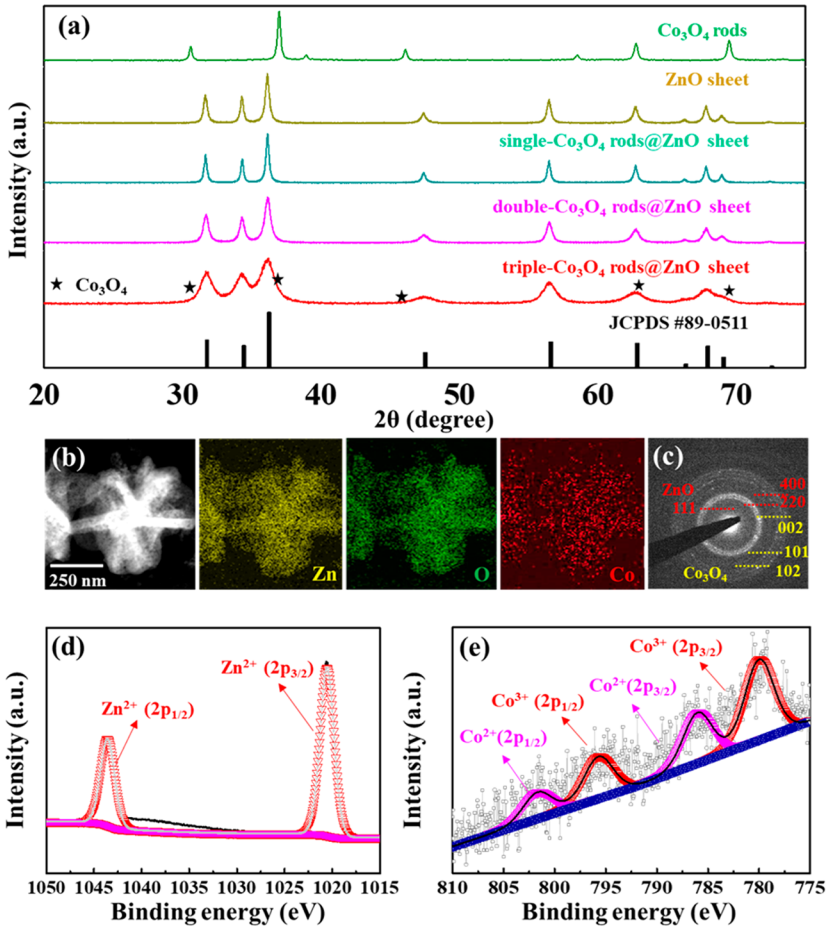

Figure 4. (a) XRD peaks of Co_3O_4 rods, ZnO sheet, single-Co_3O_4 rods@ZnO sheet, double-Co_3O_4 rods@ZnO sheet, and triple-Co_3O_4 rods@ZnO sheet. (b) EDS mapping images of triple-Co_3O_4 rods@ZnO sheet. (c) SAED pattern of triple-Co_3O_4 rods@ZnO sheet. XPS spectra of triple-Co_3O_4 rods@ZnO sheet: (d) Zn 2p, and (e) Co 2p.

rods). The combination of ZIF-67 rods and Zn-based ZIF-L induced higher $CPO_{(200)/(004)}$ (0.57) and $CPO_{(020)/(004)}$ (0.7) compared with those of pristine ZIF-L (0.362 and 0.41, respectively) (Figure S2 of the Supporting Information).

Subsequent calcination resulted in the formation of a daisy-like structure consisting of the heterogeneous Co_3O_4−ZnO composite (Figure 3a).

Interestingly, the numbers of ZIF-67 rods anchored to Zn-based ZIF-L were manipulated by using a different concentration of ZIF-67 rods dispersed in EtOH. For example, the single-ZIF-67-rod-loaded Zn-based ZIF-L was synthesized from 1.2 wt % of a ZIF-67 rod dispersed solution (Figure 3b), while the numbers of both ZIF-67 rods and Zn-based ZIF-L in hierarchical ZIF-L@ZIF-67 rods were increased in the case of using 3.5 or 7 wt % of ZIF-67 rod dispersed solution (Figure 3c,d). Numerous ZIF-67 rods are embedded within multiply assembled thin-shelled Zn-based ZIF-L. Hereafter, each ZIF-L@ZIF-67 rod corresponding to Figure 3b−d are denoted as single-ZIF-L@ZIF-67 rods, double-ZIF-L@ZIF-67 rods, and triple-ZIF-L@ZIF-67 rods. Their corresponding SEM images clearly show a different density of ZIF-67 rods on the ZIF-L (inset SEM images of Figure 3b−d). The as-prepared single-ZIF-L@ZIF-67 rods, double-ZIF-L@ZIF-67 rods, and triple-ZIF-L@ZIF-67 rods were calcined to produce heterogeneous ZnO−Co_3O_4 composites. As shown in Figure 3e, after calcination at 450 °C for 1 h, the single-Co_3O_4-rod-loaded ZnO sheet (single-Co_3O_4 rods@ZnO sheet) was successfully formed. Similarly, double-ZIF-L@ZIF-67 rods and triple-ZIF-L@ZIF-67 rods were oxidized to ZnO−Co_3O_4 composite (hereafter, double-Co_3O_4 rods@ZnO sheet and triple-Co_3O_4 rods@ZnO sheet) while maintaining their hierarchical nanostructures (Figure 3f,g).

As shown in the XRD pattern of Figure 4a, three calcined single-Co_3O_4 rods@ZnO sheet, double-Co_3O_4 rods@ZnO sheet, and triple-Co_3O_4 rods@ZnO sheet structures showed hexagonal ZnO crystallinity. The PXRD analysis of pristine Co_3O_4 rods and the pristine ZnO sheet was also carried out as reference samples. They showed characteristic XRD peaks of Co_3O_4 (JCPDS 42-1467) and ZnO (JCPDS 89-0511). However, in the case of both the single-Co_3O_4 rods@ZnO sheet and double-Co_3O_4 rods@ZnO sheet, the characteristic peaks of the Co_3O_4 phase were not observed because of the low loading amounts of Co_3O_4. On the other hand, in the case of the triple-Co_3O_4 rods@ZnO sheet, blurred XRD peaks were observed because of the overlap of characteristic Co_3O_4 peaks of (311) and (220) with ZnO peaks. To confirm the amounts of Co contents in each Co3O4 rods@ZnO sheet composite, we carried out ICP-OES (inductively coupled plasma optical emission spectroscopy) analysis by using the single-Co_3O_4 rods@ZnO sheet, double-Co_3O_4 rods@ZnO sheet, and triple-Co_3O_4 rods@ZnO sheet.

As a result, single-Co_3O_4 NRs@ZnO nanosheets and the double-Co_3O_4 rods@ZnO sheet showed relatively low Co contents (0.27% and 0.71%) in composite structures, while

DOI: 10.1021/acscentsci.8b00359
ACS Cent. Sci. 2018, 4, 929−937

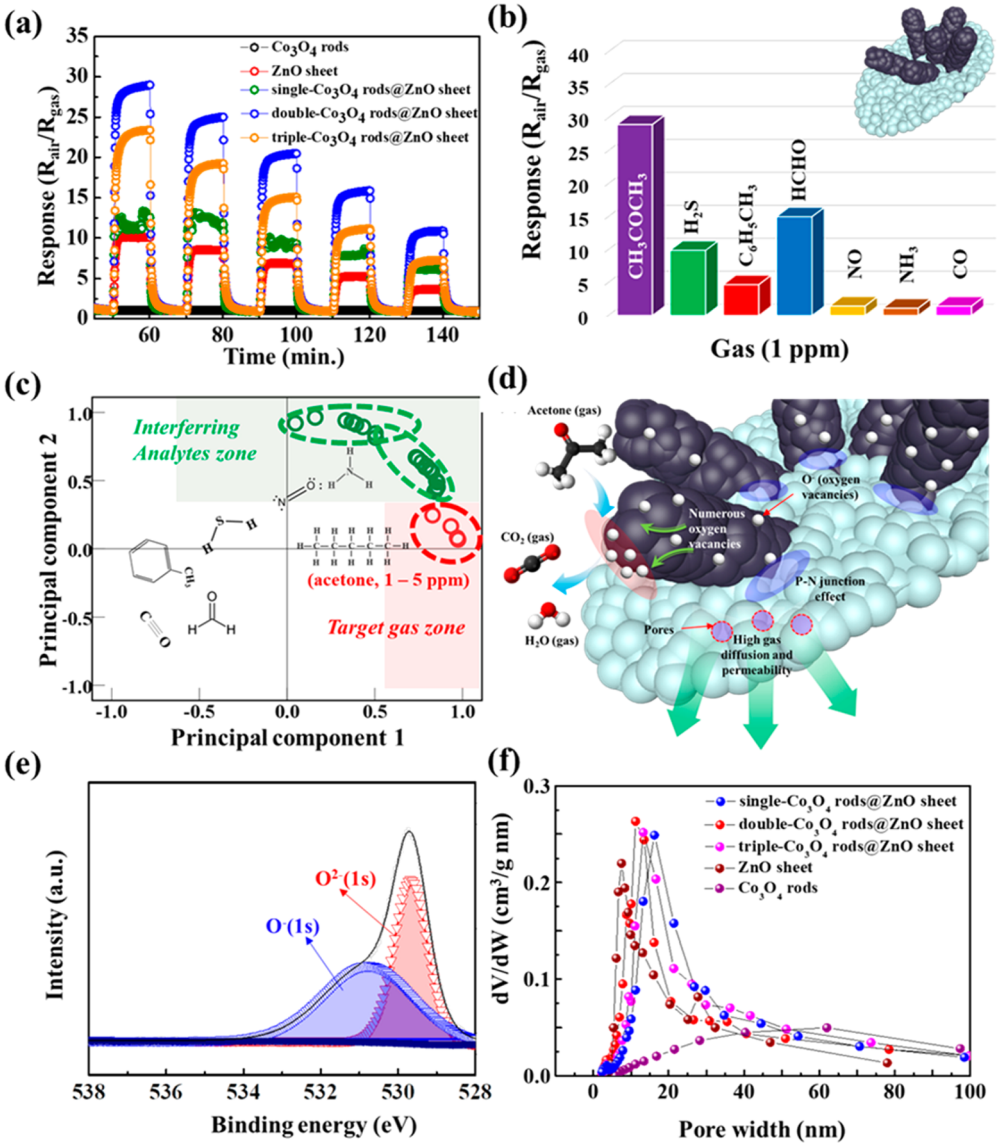

Figure 5. (a) Dynamic acetone-sensing transition in the concentration range 1−5 ppm of acetone at 450 °C. (b) Selective acetone-sensing characteristic of the double-Co_3O_4 rods@ZnO sheet against interfering analytes (H_2S, CO, toluene, HCHO, NO, and NH_3) at a concentration of 5 ppm at 450 °C. (c) Pattern recognition based on PCA using sensor arrays. (d) Suggested sensing mechanism toward acetone. (e) XPS spectra of double-Co_3O_4 rods@ZnO sheet: O 1s. (f) Pore distribution of Co_3O_4 rods, ZnO sheet, single-Co_3O_4 rods@ZnO sheet, double-Co_3O_4 rods@ZnO sheet, and triple-Co_3O_4 rods@ZnO sheet.

triple-Co_3O_4 NRs@ZnO nanosheets showed the highest Co contents (1.82%) (Table S3 of the Supporting Information). As evidence for the coexistence of ZnO and Co_3O_4, energy-dispersive X-ray spectrometer (EDS) mapping results showed a homogeneous distribution of the Co and Zn components in all composite oxide structures (Figure 4b and Figure S9 of the Supporting Information). X-ray photoelectron spectroscopy (XPS) analysis also confirmed the presence of Zn^{2+}, Co^{2+}, and Co^{3+} phases in the triple-Co_3O_4 rods@ZnO sheet (Figure 4d,e) as well as in both the single-Co_3O_4 rods@ZnO sheet and double-Co_3O_4 rods@ZnO sheet (Figure S10 of the Supporting Information). Furthermore, the selected area electron diffraction (SAED) pattern result is well-matched with XRD results (Figure 4c).

To investigate the potential feasibility of heterogeneous Co_3O_4 rods@ZnO sheets as a gas-sensing layer, we carried out gas-sensing tests toward seven different gas species, i.e., hydrogen sulfide (H_2S), acetone (CH_3COCH_3), ammonia (NH_3), carbon monoxide (CO), nitric monoxide (NO), formaldehyde (HCHO), and toluene ($C_6H_5CH_3$) under 90% relative humidity (RH) using a homemade system.[17]

As shown in Figure 5a, the double-Co_3O_4-rods@ZnO-sheet-based sensor showed the highest acetone response at 450 °C (R_{air}/R_{gas} = 29 at 5 ppm acetone, where R_{air} and R_{gas} are the resistances of sensing layers in air and target gases, respectively) compared with those of single-Co_3O_4 rods@ZnO sheets (R_{air}/R_{gas} = 12.5 at 5 ppm acetone) and triple-Co_3O_4 rods@ZnO sheets (R_{air}/R_{gas} = 23 at 5 ppm acetone). It is noted that we selected 450 °C as the optimized sensing temperature on the basis of the temperature-dependent acetone-sensing response values (Figure S11 of the Supporting Information). In addition, heterogeneous Co_3O_4 rods@ZnO sheets showed a much improved acetone response compared to the single ZnO sheet (R_{air}/R_{gas} = 10 at 5 ppm acetone) and Co_3O_4 rods (R_{air}/R_{gas} = 1.06 at 5 ppm acetone). In terms of selectivity, double-Co_3O_4 rods@ZnO sheets exhibited out-

DOI: 10.1021/acscentsci.8b00359
ACS Cent. Sci. 2018, 4, 929−937

standing acetone selectivity against interfering analytes (R_{air}/R_{gas} < 15, Figure 5b). The theoretical detection limit of the double-Co_3O_4 rods@ZnO sheets was calculated by an approximated linear plot as a function of acetone concentration, considering the noise level of the base resistances (Figure S12 of the Supporting Information).[27] The detection limit of double-Co_3O_4 rods@ZnO sheet level is 5 ppb level acetone concentration with apparent response (R_{air}/R_{gas} = 1.04). Although the double-Co_3O_4 rods@ZnO sheets also showed a relatively high response toward HCHO (R_{air}/R_{gas} = 15), the selectivity toward the two gases can be clearly distinguished using the sensor arrays. To further improve the acetone selectivity of our sensor arrays, i.e., single-Co_3O_4 rods@ZnO sheets, double-Co_3O_4 rods@ZnO sheets, and triple-Co_3O_4 rods@ZnO sheets, we carried out principal component analysis (PCA), which is widely used as a pattern recognition tool.[28] As a result, the 6 interfering gas molecules and acetone gas were clearly classified to two clusters (red dotted region and green dotted regions) even at a highly humid state (90 RH%) in the 2D space (Figure 5c). According to previous studies, ppm level acetone gas molecules in human breath, having a high humidity level (>90 RH%), is strongly related with diabetes and fat-burning. Thus, our HMOF-derived heterogeneous sensing layers including single-Co_3O_4 rods@ZnO sheets, double-Co_3O_4 rods@ZnO sheets, and triple-Co_3O_4 rods@ZnO sheets can be potentially applied to a breath analyzer for human health care.

The improved acetone-sensing characteristics are attributed to the (i) creation of p−n heterointerfaces, (ii) catalytic effect of Co_3O_4 rods on 2D ZnO sheet, and (iii) highly porous nanostructures. First, p−n junctions are formed at the interface between p-type Co_3O_4 rods and the n-type ZnO sheet (blue ellipses in Figure 5d); the p−n junctions resulted in the formation of a larger electron depletion region, leading to sensitive resistance variation when target gases are exposed to sensing layers. Thus, the thickness of the electron depletion region formed at the interface between Co_3O_4 rods and the ZnO sheet can be hugely modulated (thinned), inducing a rapid decrease of resistance. The higher base resistance of the double-Co_3O_4 rods@ZnO sheet (8 MΩ) compared with those of pristine Co_3O_4 rods (2.08 kΩ) and the ZnO sheet (6 MΩ) supports that the p−n heterojunctions were built between p-type Co_3O_4 rods and the n-type ZnO sheet (Figure S9 of the Supporting Information). Furthermore, the baseline resistance of Co_3O_4 rods@ZnO sheet composite structures is proportional to the amount of Co_3O_4 in the Co_3O_4 rods@ZnO sheet composite because of the large number of p−n junctions between p-type Co_3O_4 rods and the n-type ZnO sheet (Figure S13 of the Supporting Information).

Second, catalytic Co_3O_4 rods immobilized on the ZnO sheet possess many oxygen vacancies which are inherently generated in spinel Co_3O_4 structure. The multivalence nature of the Co (Co^{2+} and Co^{3+}) component in spinel Co_3O_4 induces the generation of oxygen vacancies on the Co_3O_4 surface,[29] leading to enhanced gas reaction sites (red ellipses in Figure 5d). Furthermore, catalytic Co_3O_4 is a widely known effective material for selective activation of the reaction between acetone and chemisorbed oxygen species when introduced on metal oxides.[28,30−32] Since the sensing reaction is based on the chemical interaction between acetone molecules and chemisorbed oxygen species as expressed in eq 1, a larger amount of chemisorbed oxygen (O^-) species adsorbed on the sensing layers are advantageous to improve the sensitivity.[16] As shown in the XPS spectra of the double-Co_3O_4 rods@ZnO sheet (Figure 5e), the peaks of chemisorbed oxygen (O^- and O^{2-}) were clearly observed at binding energies of 530.2 and 531.0 eV, respectively.[33] The ratio of O^-/O^{2-} (1.203) in the double-Co_3O_4 rods@ZnO sheet was much higher than those of the single-Co_3O_4 rods@ZnO sheet (0.615) and triple-Co_3O_4 rods@ZnO sheet (0.727) (Table S4 and Figure S14 of the Supporting Information). On the basis of the peak ratio of chemisorbed oxygen in the sensing layers, the double-Co_3O_4 rods@ZnO sheets are an optimized acetone-sensing layer among different Co_3O_4-loaded Co_3O_4 rods@ZnO sheet composites.

$$CH_3COCH_3(gas) + 8O^- \rightarrow 3H_2O + 3CO_2 + 8e^- \quad (1)$$

Third, the meso-sized pores created on the thin-walled ZnO sheet also contribute an enhanced gas-sensing performance by facilitating gas permeability dominated by Knudsen diffusion (purple circles in Figure 5d). We measured the pore size distribution of Co_3O_4 rods, ZnO sheet, single-Co_3O_4 rods@ZnO sheet, double-Co_3O_4 rods@ZnO sheet, and triple-Co_3O_4 rods@ZnO sheet (Figure 5f). The double-Co_3O_4 rods@ZnO sheet showed the highest pore volume (0.123 cm^3/g) with meso-sized mean pore diameter (12.630 nm) compared with those of ZnO sheet (0.115 cm^3/g), Co_3O_4 rods (0.043 cm^3/g), single-Co_3O_4 rods@ZnO sheet (0.111 cm^3/g), and triple-Co_3O_4 rods@ZnO sheet (0.117 cm^3/g). Furthermore, the highest BET surface area of the double-Co_3O_4 rods@ZnO sheet was observed (31.220 m^2/g) compared with those of other samples: single-Co_3O_4 rods@ZnO sheet (22.372 m^2/g) and triple-Co_3O_4 rods@ZnO sheet (25.367 m^2/g) (Figure S15 of the Supporting Information). On the basis of improved pore size distribution and surface area, the double-Co_3O_4 rods@ZnO sheet can show the most sensitive acetone-sensing characteristics. Considering the comparison data with state-of-the-art MOF-templated acetone-gas-sensor works collected from previous reports (Tables S5 and S6 of the Supporting Information), our double-Co_3O_4 rods@ZnO sheets show superior gas-sensing results.

CONCLUSIONS

In summary, we synthesized variously shaped ZIF-67 and ZIF-8, including polyhedron, sheet, rod, and belt, by controlling the relative ratio of two mixed solvents, EtOH and DI water. Heterogeneous 1D Co_3O_4-rod-loaded 2D ZnO sheets were achieved via in situ coupling of sheet-shaped Zn-based ZIF-L and rod-shaped ZIF-67 followed by high-temperature calcination. Because of the (i) heterojunction p−n junction effect, (ii) catalytic effect of Co_3O_4, and (iii) porous structure of hybrid-MOF-templated Co_3O_4 rods@ZnO sheet, significantly enhanced acetone-sensing properties were achieved. With this strategy, one can rationally design the desired heterogeneous composite structures with diverse MOF morphologies, which are highly suitable not only for chemical sensors but also for other applications such as catalysis and energy storage.

EXPERIMENTAL SECTION

Materials. Cobalt nitrate hexahydrate ($Co(NO_3)_2·6H_2O$), zinc nitrate hexahydrate ($Zn(NO_3)_2·6H_2O$), 2-methylimidazole (HMIM, $C_4H_6N_2$, 99.0%), and absolute ethanol (CH_3CH_2OH, EtOH) were purchased from Sigma-Aldrich (St. Louis, MO). All chemicals were used without further

DOI: 10.1021/acscentsci.8b00359
ACS Cent. Sci. 2018, 4, 929−937

purification. No unexpected or unusually high safety hazards were encountered in any of the experimental procedures.

Synthesis of Polyhedral ZIF-67, Co-Based ZIF-L, ZIF-67 Rods, and ZIF-67 Belts. First, conventional polyhedral ZIF-67 was synthesized by using methanol solvent. A 0.3 g portion of cobalt nitrate hexahydrate and 0.65 g of HMIM were separately dissolved in 20 mL of methanol to prepare two solutions (Co-ion-dissolved methanol and HMIM-dissolved methanol). The two as-prepared solutions were mixed and vigorously stirred for 3 h at room temperature. Afterward, the obtained purple solution was purified two times by centrifugation (3000 rpm for 10 min). Then, the obtained sediment was dried at 50 °C for 24 h. Second, nanosheet-shaped ZIF-L was prepared in DI water. Similarly, 0.3 g of cobalt nitrate hexahydrate and 0.65 g of HMIM were separately dissolved in 20 mL of DI water. The two solutions were mixed and stirred for 3 h at room temperature. The washing and collection processes of ZIF-L were conducted in the same condition. Lastly, ZIF-67 rods and ZIF-67 belts were synthesized by using the mixed cosolvent of EtOH and DI water. In the case of ZIF-67 rods, 0.3 g of cobalt nitrate hexahydrate was dissolved in the 27 mL of DI water while 0.65 g of HMIM was dissolved in 13 mL of EtOH. Afterward, HMIM-dissolved EtOH solution was gently poured into the cobalt-nitrate-hexahydrate-dissolved DI water and stirred for 3 h at room temperature. In the case of ZIF-67 belts, 0.3 g of cobalt nitrate hexahydrate was dissolved in 13 mL of DI water while 0.65 g of HMIM was dissolved in 27 mL of EtOH. Then, the EtOH-based solution was also poured into the DI-water-based solution and stirred for 3 h at room temperature. It is noted that the washing and collection processes of ZIF-67 rods and ZIF-67 belts were also the same as in the above method.

Synthesis of HMOF and HMOF-Driven Heterogeneous ZnO/Co_3O_4 Hierarchical Structures. Solutions of 1.2, 3.5, and 7 wt % of as-prepared ZIF-67 rods were dispersed in 20 mL of DI water, respectively. Then, 0.3 g of zinc nitrate hexahydrate was dissolved in DI water solution including the as-prepared ZIF-67 rods. Meanwhile, 0.65 g of zinc nitrate hexahydrate was dissolved in 20 mL of DI water. The two solutions were mixed and gently stirred for 3 h. The as-prepared lilac solution was purified by centrifugation at 3000 rpm for 5 min. Then, the lilac sediment was washed by EtOH and fully dried at 50 °C for 12 h. To achieve the heterogeneous 1D Co_3O_4-rod-embedded 2D ZnO sheet, which includes the single-Co_3O_4 rods@ZnO sheet, double-Co_3O_4 rods@ZnO sheet, and triple-Co_3O_4 rods@ZnO sheet, three lilac powders having different concentrations of ZIF-67 rods were calcined at 450 °C for 1 h with a ramping rate 5 °C/min. Three different powders showed yellow−green colors with different brightness, having hierarchical ZnO/Co_3O_4 composite structures.

Material Characterization. The morphologies of each sample were examined by field-emission scanning electron microscopy (FE-SEM, Nova 230). The microstructure, selected area electron diffraction (SAED) pattern, and EDS mapping analysis of each sample were analyzed by transmission electron microscopy (TEM) (Tecnai F30 S-Twin, FEI). The crystal structure of each sample was observed by X-ray diffraction (XRD) pattern with an X-ray diffractometer (D/MAX-RC 12 kW, Rigaku) using Cu Kα (λ = 1.54 Å) radiation. The chemical bonding states of Co, Zn, and O in HMOF-derived metal oxide were investigated by X-ray photoelectron spectroscopy (XPS, Sigma Probe, Thermo VG Scientific) with Al Kα radiation (1486.6 eV). Sensing properties of the ZnO sheet, Co_3O_4 rods, single-Co_3O_4 rods@ZnO sheet, double-Co_3O_4 rods@ZnO sheet, and triple-Co_3O_4 rods@ZnO sheet were evaluated by homemade testing equipment described elsewhere. The resistance variation of each sample was measured by using a data acquisition system (34972A, Agilent).

■ ASSOCIATED CONTENT

Supporting Information

The Supporting Information is available free of charge on the ACS Publications website at DOI: 10.1021/acscentsci.8b00359.

Additional data including pH values, grain sizes, ICP results, surface areas, and sensor properties and additional images including TEM and SEM images, EDS mapping images, schematic illustrations, XRD, temperature-dependent acetone response, detection limits, resistance variations, and N_2 adsorption/desorption isotherms (PDF)

■ AUTHOR INFORMATION

Corresponding Author

*E-mail: idkim@kaist.ac.kr.

ORCID

Il-Doo Kim: 0000-0002-9970-2218

Notes

The authors declare no competing financial interest.

■ ACKNOWLEDGMENTS

This work was supported by Wearable Platform Materials Technology Center (WMC) funded by National Research Foundation of Korea (NRF) Grant of the Korean Government (MSIP) (2016R1A5A1009926). This work was also supported by the National Research Foundation of Korea (NRF), Grant 2014R1A4A1003712 (BRL Program). This research was supported by Multi-Ministry Collaborative R&D Program (Development of Techniques for Identification and Analysis of Gas Molecules to Protect Against Toxic Substances) through the National Research Foundation of Korea (NRF) funded by KNPA, MSIT, MOTIE, ME, and NFA (2017M3D9A1073501). This work supported by the center for Integrated Smart Sensors funded by Global Ph.D Fellowship Program through the National Research Foundation of Korea (NRF) funded by the Ministry of Education (No. NRF2016H1A2A1907718).

■ REFERENCES

(1) Kaneti, Y. V.; Tang, J.; Salunkhe, R. R.; Jiang, X.; Yu, A.; Wu, K. C. W.; Yamauchi, Y. Nanoarchitectured Design of Porous Materials and Nanocomposites from Metal-Organic Frameworks. *Adv. Mater.* **2017**, *29*, 1604898.

(2) Xia, W.; Zou, R.; An, L.; Xia, D.; Guo, S. A Metal−Organic Framework Route to In situ Encapsulation of Co@Co_3O_4@C core@Bishell Nanoparticles into a Highly Ordered Porous Carbon Matrix for Oxygen Reduction. *Energy Environ. Sci.* **2015**, *8*, 568−576.

(3) Zhao, S.; Yin, H.; Du, L.; He, L.; Zhao, K.; Chang, L.; Yin, G.; Zhao, H.; Liu, S.; Tang, Z. Carbonized Nanoscale Metal−Organic Frameworks as High Performance Electrocatalyst for Oxygen Reduction Reaction. *ACS Nano* **2014**, *8*, 12660−12668.

(4) Zhang, Y.; Guo, J.; Shi, L.; Zhu, Y.; Hou, K.; Zheng, Y.; Tang, Z. Tunable Chiral Metal Organic Frameworks Toward Visible Light−Driven Asymmetric Catalysis. *Sci. Adv.* **2017**, *3*, e1701162.

DOI: 10.1021/acscentsci.8b00359
ACS Cent. Sci. 2018, 4, 929−937

(5) Zhao, M.; Yuan, K.; Wang, Y.; Li, G.; Guo, J.; Gu, L.; Hu, W.; Zhao, H.; Tang, Z. Metal−Organic Frameworks as Selectivity Regulators for Hydrogenation Reactions. *Nature* **2016**, *539*, 76.
(6) Yang, D.-A.; Cho, H.-Y.; Kim, J.; Yang, S.-T.; Ahn, W.-S. CO_2 Capture and Conversion Using Mg-MOF-74 Prepared by a Sonochemical Method. *Energy Environ. Sci.* **2012**, *5*, 6465−6473.
(7) Zhang, G.; Hou, S.; Zhang, H.; Zeng, W.; Yan, F.; Li, C. C.; Duan, H. High-Performance and Ultra-Stable Lithium-Ion Batteries Based on MOF-Derived ZnO@ ZnO Quantum Dots/C Core−Shell Nanorod Arrays on a Carbon Cloth Anode. *Adv. Mater.* **2015**, *27*, 2400−2405.
(8) Li, X.; Hao, C.; Tang, B.; Wang, Y.; Liu, M.; Wang, Y.; Zhu, Y.; Lu, C.; Tang, Z. Supercapacitor Electrode Materials with Hierarchically Structured Pores from Carbonization of MWCNTs and ZIF-8 Composites. *Nanoscale* **2017**, *9*, 2178−2187.
(9) Horcajada, P.; Chalati, T.; Serre, C.; Gillet, B.; Sebrie, C.; Baati, T.; Eubank, J. F.; Heurtaux, D.; Clayette, P.; Kreuz, C. Porous Metal−Organic-Framework Nanoscale Carriers as a Potential Platform for Drug Delivery and Imaging. *Nat. Mater.* **2010**, *9*, 172.
(10) Koo, W.-T.; Choi, S.-J.; Kim, S.-J.; Jang, J.-S.; Tuller, H. L.; Kim, I.-D. Heterogeneous Sensitization of Metal−Organic Framework Driven Metal@ Metal Oxide Complex Catalysts on an Oxide Nanofiber Scaffold Toward Superior Gas Sensors. *J. Am. Chem. Soc.* **2016**, *138*, 13431−13437.
(11) Guo, W.; Sun, W.; Lv, L.-P.; Kong, S.; Wang, Y. Microwave-Assisted Morphology Evolution of Fe-Based Metal−Organic Frameworks and Their Derived Fe_2O_3 Nanostructures for Li-Ion Storage. *ACS Nano* **2017**, *11*, 4198−4205.
(12) Zhao, S.; Wang, Y.; Dong, J.; He, C.-T.; Yin, H.; An, P.; Zhao, K.; Zhang, X.; Gao, C.; Zhang, L. Ultrathin Metal−Organic Framework Nanosheets for Electrocatalytic Oxygen Evolution. *Nat. Energy* **2016**, *1*, 16184.
(13) Guan, B. Y.; Yu, L.; Lou, X. W. D. A Dual-Metal−Organic-Framework Derived Electrocatalyst for Oxygen Reduction. *Energy Environ. Sci.* **2016**, *9*, 3092−3096.
(14) Edmonds, J.; Reilly, J. A Long-term Global Energy-economic Model of Carbon Dioxide Release from Fossil Fuel Use. *Energy Economics* **1983**, *5*, 74−88.
(15) Barea, E.; Montoro, C.; Navarro, J. A. Toxic Gas Removal−Metal−Organic Frameworks for the Capture and Degradation of Toxic Gases and Vapours. *Chem. Soc. Rev.* **2014**, *43*, 5419−5430.
(16) Kim, S. J.; Choi, S. J.; Jang, J. S.; Cho, H. J.; Koo, W. T.; Tuller, H. L.; Kim, I. D. Exceptional High-Performance of Pt-Based Bimetallic Catalysts for Exclusive Detection of Exhaled Biomarkers. *Adv. Mater.* **2017**, *29*, 1700737.
(17) Jang, J. S.; Choi, S. J.; Kim, S. J.; Hakim, M.; Kim, I. D. Rational Design of Highly Porous SnO_2 Nanotubes Functionalized with Biomimetic Nanocatalysts for Direct Observation of Simulated Diabetes. *Adv. Funct. Mater.* **2016**, *26*, 4740−4748.
(18) Chen, R.; Yao, J.; Gu, Q.; Smeets, S.; Baerlocher, C.; Gu, H.; Zhu, D.; Morris, W.; Yaghi, O. M.; Wang, H. A Two-dimensional Zeolitic Imidazolate Framework with a Cushion-Shaped Cavity for CO_2 Adsorption. *Chem. Commun.* **2013**, *49*, 9500−9502.
(19) Liu, Q.; Low, Z.-X.; Feng, Y.; Leong, S.; Zhong, Z.; Yao, J.; Hapgood, K.; Wang, H. Direct Conversion of Two-dimensional ZIF-L Film to Porous ZnO Nano-sheet Film and its Performance as Photoanode in Dye-sensitized Solar Cell. *Microporous Mesoporous Mater.* **2014**, *194*, 1−7.
(20) Cai, Y.; Zhang Newby, B.-m. Marangoni Flow-induced Self-assembly of Hexagonal and Stripelike Nanoparticle Patterns. *J. Am. Chem. Soc.* **2008**, *130*, 6076−6077.
(21) Yang, J.; Zhang, F.; Lu, H.; Hong, X.; Jiang, H.; Wu, Y.; Li, Y. Hollow Zn/Co ZIF Particles Derived from Core−Shell ZIF-67@ ZIF-8 as Selective Catalyst for the Semi-Hydrogenation of Acetylene. *Angew. Chem., Int. Ed.* **2015**, *54*, 10889−10893.
(22) Tang, J.; Salunkhe, R. R.; Liu, J.; Torad, N. L.; Imura, M.; Furukawa, S.; Yamauchi, Y. Thermal Conversion of Core−shell Metal−organic Frameworks: a New Method for Selectively Functionalized Nanoporous Hybrid Carbon. *J. Am. Chem. Soc.* **2015**, *137*, 1572−1580.
(23) Xu, C.; Tamaki, J.; Miura, N.; Yamazoe, N. Grain size effects on gas sensitivity of porous SnO2-based elements. *Sens. Actuators, B* **1991**, *3*, 147−155.
(24) Rothschild, A.; Komem, Y. The effect of grain size on the sensitivity of nanocrystalline metal-oxide gas sensors. *J. Appl. Phys.* **2004**, *95*, 6374−6380.
(25) Sakai, G.; Matsunaga, N.; Shimanoe, K.; Yamazoe, N. Theory of Gas-Diffusion Controlled Sensitivity for Thin Film Semiconductor Gas Sensor. *Sens. Actuators, B* **2001**, *80*, 125−131.
(26) Sberveglieri, G. Recent Developments in Semiconducting Thin-Film Gas Sensors. *Sens. Actuators, B* **1995**, *23*, 103−109.
(27) Kim, I.-D.; Rothschild, A.; Lee, B. H.; Kim, D. Y.; Jo, S. M.; Tuller, H. L. Ultrasensitive Chemiresistors Based on Electrospun TiO_2 Nanofibers. *Nano Lett.* **2006**, *6*, 2009−2013.
(28) Jang, J.-S.; Koo, W.-T.; Choi, S.-J.; Kim, I.-D. Metal Organic Framework-Templated Chemiresistor: Sensing Type Transition from P-to-N Using Hollow Metal Oxide Polyhedron via Galvanic Replacement. *J. Am. Chem. Soc.* **2017**, *139*, 11868−11876.
(29) Xu, L.; Jiang, Q.; Xiao, Z.; Li, X.; Huo, J.; Wang, S.; Dai, L. Plasma-Engraved Co_3O_4 Nanosheets with Oxygen Vacancies and High Surface Area for the Oxygen Evolution Reaction. *Angew. Chem.* **2016**, *128*, 5363−5367.
(30) Zhang, Z.; Zhu, L.; Wen, Z.; Ye, Z. Controllable synthesis of Co_3O_4 crossed Nanosheet Arrays Toward an Acetone Gas Sensor. *Sens. Actuators, B* **2017**, *238*, 1052−1059.
(31) Rahman, M. M.; Khan, S. B.; Asiri, A. M.; Alamry, K. A.; Khan, A. A. P.; Khan, A.; Rub, M. A.; Azum, N. Acetone sensor based on solvothermally prepared ZnO doped with Co_3O_4 nanorods. *Microchim. Acta* **2013**, *180*, 675−685.
(32) Qu, F.; Liu, J.; Wang, Y.; Wen, S.; Chen, Y.; Li, X.; Ruan, S. Hierarchical Fe_3O_4@ Co_3O_4 Core−Shell Microspheres: Preparation and Acetone Sensing Properties. *Sens. Actuators, B* **2014**, *199*, 346−353.
(33) Jang, J.-S.; Kim, S.-J.; Choi, S.-J.; Kim, N.-H.; Hakim, M.; Rothschild, A.; Kim, I.-D. Thin-walled SnO_2 nanotubes functionalized with Pt and Au catalysts via the protein templating route and their selective detection of acetone and hydrogen sulfide molecules. *Nanoscale* **2015**, *7*, 16417−16426.

DOI: 10.1021/acscentsci.8b00359
ACS Cent. Sci. 2018, 4, 929−937